CHEMICAL PHYSICS

Electrocatalytic polyvinylidene fluoride defluorination with water mediation at room temperature

Yifan Bu[1]†, Peixuan Li[2,3]†, Xiayu Yuan[4]†, Lei Tao[3], Chengcheng Ji[4], Junzhong Xie[1], Yao Xu[1], Shixuan Du[2,3]*, Wulin Yang[4]*, Mufan Li[1]*

Polyvinylidene fluoride (PVDF), a widely used recalcitrant per- and polyfluoroalkyl substance (PFAS) polymer, poses environmental challenges in its defluorination because conventional thermal methods release toxic volatile fluorinated compounds (VFCs). Here, we report an electrochemical water-mediated strategy for efficient, VFC-free PVDF defluorination under ambient conditions. The method achieves a high fluorine-to-fluoride conversion (93%) and is validated with an industrially relevant capacity of 8.5 kg·m^{-3}·day^{-1} on real wasted battery electrodes containing PVDF as the binder. The high efficiency originates from the spatial confinement of electrochemically generated hydroxide ions near the cathode surface. Mechanistically, isotopic labeling and kinetic Monte Carlo simulations reveal water's unprecedented dual role as both a reactant and a catalyst, driving an ionic pathway that fundamentally suppresses VFCs. This offers a scalable, sustainable, and nontoxic alternative for the critical challenge of C—F breaking and PFAS defluorination.

INTRODUCTION

Polyvinylidene fluoride (PVDF) is a polymeric per- and polyfluoroalkyl substance (PFAS), with broad use as the binder and membrane in batteries, films, wire insulation, and architectural coatings (*1*–*6*), which presents substantial environmental challenges during its treatment (*7*, *8*). The dominant industrial strategy for treating PVDF is pyrolysis (Fig. 1A) (*9*, *10*), which is highly energy-intensive and, more critically, drives the thermal decomposition of PVDF, leading to the emission of toxic volatile fluorinated compounds (VFCs) (*7*, *11*, *12*). Life cycle assessment indicates that the released VFCs contribute to global warming impacts orders of magnitude more severe than those of CO_2 and methane (fig. S1) (*13*), underscoring the urgent need for VFC-free PVDF defluorination technologies.

Although considerable efforts have been devoted to realizing the effective degradation of persistent PFAS, the harsh degradation conditions, such as high temperature (*14*–*16*) and high pressure (*15*), ball milling (*17*–*20*), highly active reductants (*18*), or advanced photocatalysis under strictly controlled anhydrous and oxygen-free environments (*21*, *22*), are prohibitively difficult to achieve, hindering their scalable implementation. Electrochemistry provides a viable pathway for defluorination, enabling C—F bond cleavage through precise potential control at room temperature and atmospheric pressure. Nevertheless, the intrinsic stability of the C—F bond typically necessitates high potentials to drive charge transfer (*23*) or to generate highly reactive defluorinating intermediates (*24*) and occasionally leads to insufficient defluorination efficiency (*25*). The integration of chemical and electrochemical processes presents a promising alternative, where electrochemically generated active species are concentrated near the electrode surface, enhancing the reaction kinetics, limiting the diffusion of corrosive pollutants, and mitigating the reactor corrosion (*26*). Water, as an inexpensive and environmentally benign species, can be electrochemically activated to highly reactive species at mild conditions (*27*), such as O (*28*, *29*), OH (*28*), and O_2 (*30*), thereby promoting subsequent chemical reactions. For example, reactive oxygen species produced through water oxidation or oxygen reduction have been effectively used to degrade water-soluble, small-molecule PFAS (*31*). However, the electrochemical full defluorination of polymeric PFAS, such as PVDF, under mild conditions remains unrealized (*32*).

Here, we presented a simple electrochemical water-mediated strategy for PVDF defluorination at room temperature via integrating chemical and electrochemical processes (Fig. 1B), which is then further applied to real battery recycling scenarios with a designed scaled-up device as the practical demonstration. Cathodic reduction of water produced H_2 and hydroxide ions, with the latter reacting with PVDF to initiate defluorination. The spatial confinement of hydroxide ions near the electrode suppressed corrosion and improved efficiency. Through the design of reaction pathway, we realized the degradation of PVDF through an ionic process, unlike the free-radical process enabled by high-temperature (*33*) in the pyrolysis approach, thereby effectively circumventing the formation of VFCs (Fig. 1C). In a lab-scale electrochemical system, a Faradaic efficiency (FE) of 93% and a fluoride production rate of 0.28 mmol hour^{-1} were achieved, with 93% of the fluorine in PVDF converted to fluoride ions. Isotopic labeling experiments and ab initio kinetic Monte Carlo simulations revealed that water serves dual roles as both catalyst and reactant, operating through two parallel pathways: water catalysis and water reaction, collectively termed the "water-mediated" pathways. By integrating this method into a customized reactor, we achieved a processing capacity of 8.5 kg m^{-3} day^{-1} with a defluorination efficiency of over 90%, and realized complete elimination of VFCs emissions while preserving the structural integrity of the battery materials with a recycle efficiency of 98.1%, demonstrating one of the industrial application scenarios along this route.

[1]College of Chemistry and Molecular Engineering, Peking University, Beijing 100871, China. [2]Beijing National Laboratory for Condensed Matter Physics, Institute of Physics, Chinese Academy of Sciences, Beijing 100190, China. [3]School of Physics, University of Chinese Academy of Sciences, Beijing 100049, China. [4]The Key Laboratory of Water and Sediment Sciences, Ministry of Education; College of Environmental Sciences and Engineering, Peking University, Beijing 100871, China.
*Corresponding author. Email: sxdu@iphy.ac.cn (S.D.); wulin.yang@pku.edu.cn (W.Y.); mufanli@pku.edu.cn (M.L.).
†These authors contributed equally to this work.

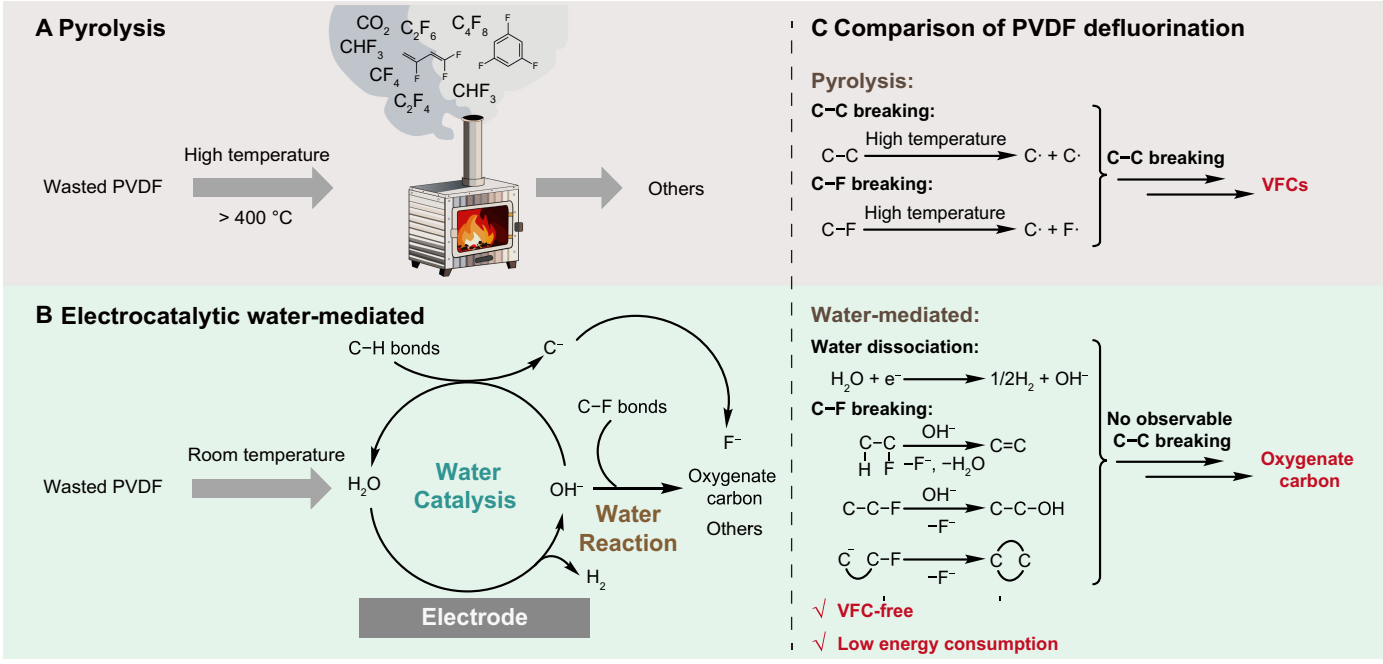

Fig. 1. Development of methods for PVDF defluorination. (**A**) Pyrolysis PVDF defluorination. (**B**) Electrocatalytic water-mediated PVDF defluorination. (**C**) Comparison of two PVDF defluorination approaches.

RESULTS

Concept validation and performance evaluation

We began with designing the water-mediated pathway for PVDF defluorination, as illustrated in Fig. 2A, and experimentally validated this concept at the lab scale. Forty-five solvents, such as water, ethanol, and *N*,*N*-dimethylacetamide (DMAc), were screened, and DMAc was identified as the most effective medium for defluorination (table S1). X-ray photoelectron spectroscopy (XPS) analysis of the carbonaceous solids products showed a notable shift in the carbon-to-fluorine ratio, which increased from approximately 1 to 60 after the reaction, as evidenced by the C 1s peak (around 285 eV) and F 1s peak (around 685 eV) on the survey spectra (fig. S2), indicating the successful defluorination. High-resolution XPS spectra of F 1s and C 1s provided further insights into the product's structure (Fig. 2B). The characteristic F 1s peak of the $[—CH_2—CF_2—]_n$ structure at 689.8 eV disappeared after the reaction, and was replaced by a new peak corresponding to F^- (683.5 eV), verifying the formation of fluoride and the cleavage of C—F bonds. This was also supported by the infrared and Raman spectra after the reaction (figs. S3 and S4) (*34*). The peak around 688.2 eV was attributed to fluorine of the $[—CH═CF—]_n$ structure in the carbonaceous solids. On the C 1s spectrum, oxygen-containing functional groups, C—OH (285.5 eV) and C═O (286.5 eV), were identified, indicating the incorporation of oxygen in water into the defluorinated PVDF. Powder x-ray diffraction (XRD) patterns showed no crystalline phases, indicating the amorphous nature of the product (fig. S5). Transmission electron microscopy revealed particles with sizes around 3 to 4 nm (fig. S6). Together, these results demonstrate efficient cleavage of C—F bonds in PVDF, leading to the formation of oxygen-functionalized amorphous carbonaceous solids along with fluoride ions.

To optimize the reaction conditions, we first investigated the effect of temperature. Both the FE and productivity increased with temperature rising to 60°C, above which they plateaued (fig. S7). This observation can be attributed to the thermal activation of the defluorination process at temperatures below 60°C, whereas at elevated temperatures, the overall efficiency is compromised by the intensification of competitive pathways, including solvent hydrolysis and the crossover of anodic species (refer to figs. S8 and S9 for detailed analysis). The cell voltage decreased as the temperature rose (fig. S10), which can be attributed to reduced cell resistance (fig. S11) and enhanced reaction kinetics (fig. S10). Then we evaluated the effect of current density (Fig. 2C). The productivity increased as the current density rose. FE was also promoted at higher current densities and remained relatively constant beyond 10 mA cm^{-2}, reaching a maximum above 90%, suggesting that elevated concentrations of electrochemically generated intermediates contribute to higher reaction efficiency. The current density beyond which the FE remained relatively constant could be affected by the concentration of the reactant, which will be decreased with a lower concentration of H_2O or a higher concentration of PVDF (fig. S12). Kinetic analysis at various temperatures under nonelectrochemical conditions revealed a near-second-order dependence on hydroxide ions. (Fig. 2D), corroborating the positive correlation between current density and FE (refer to fig. S13 and note S1 for detailed analysis). The activation energy for the defluorination reaction was determined to be 5.2 kcal·mol^{-1} (Fig. 2E), indicating that the process proceeds readily near room temperature. Under optimal conditions, 93% of the fluorine in 640 mg of PVDF was converted to F^-, with a carbon balance of 97% (Fig. 2F). We performed 21 consecutive reaction cycles using the same electrolytic cell, with the defluorination efficiency consistently remaining above 90%, demonstrating the stability of our reaction system (fig. S14). Furthermore, the strategy demonstrated broad applicability across different electrolyte salts and diverse electrode materials (figs. S15 and S16).

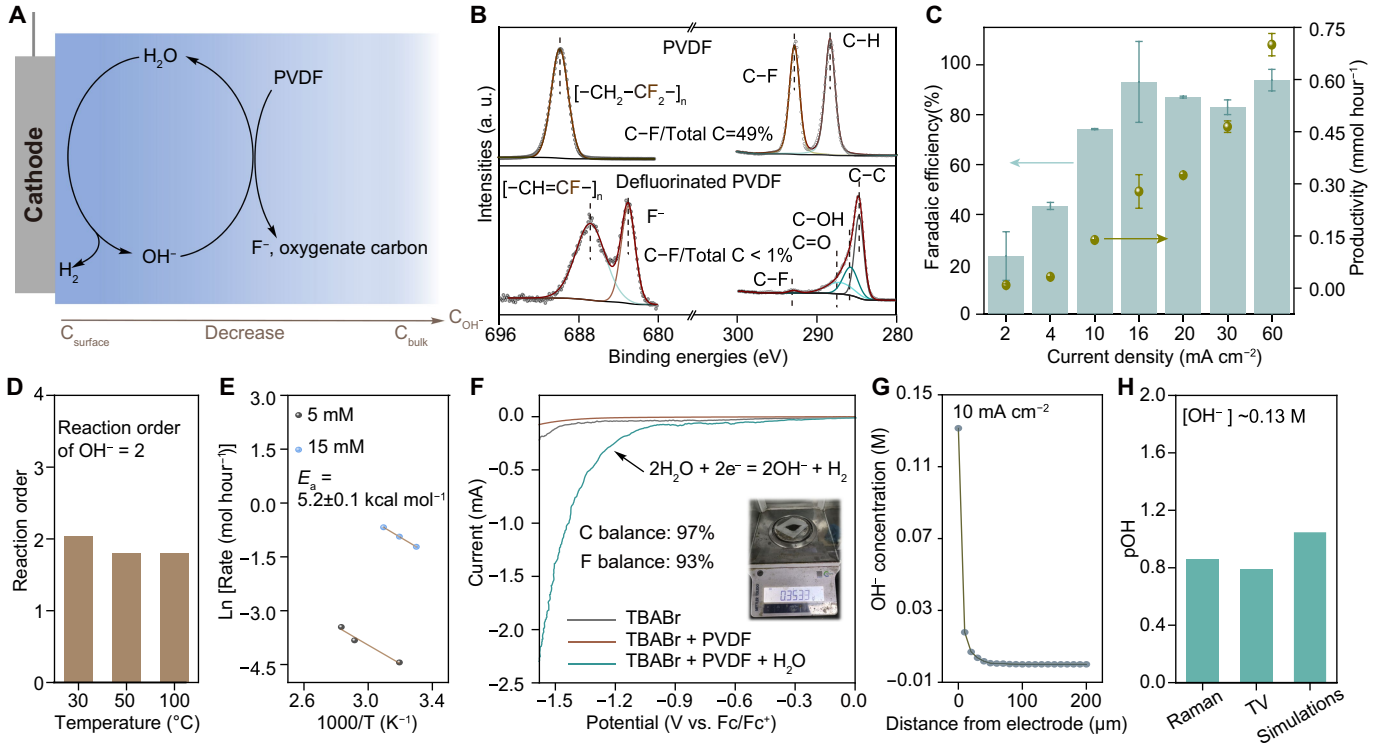

Fig. 2. Performance evaluation of water-mediated PVDF defluorination. (**A**) Illustration of the defluorination system and demonstration of spatially confined highly concentrated hydroxide ions. (**B**) F 1s (The lower signal-to-noise ratio indicates the successful reduction of the total amount of fluorine) and C 1s XPS spectra of PVDF and defluorinated PVDF. (**C**) FE and productivity of electrochemical water-mediated PVDF defluorination at different current densities (electrolyte: 0.1 M TBAB + 0.5 M H_2O + 0.1 M PVDF in DMAc. Each experiment was run three times, and the average is shown. The area of the electrode was 0.5 cm^{-2}). (**D**) Reaction order and (**E**) activation energy of the reaction under nonelectrochemical conditions (each experiment was run three times, and the final data are fitted and calculated with the averaged concentration). (**F**) Linear sweep voltammetry with or without PVDF and water (Insets are the carbon balance and fluorine balance in a lab-scale experiment with 640 mg PVDF). (**G**) Distribution of OH^- concentration near the electrode measured with SECM. (**H**) Local OH^- concentration measured with in situ Raman spectroscopy, transient voltage measurements, and its simulations.

Linear sweep voltammetry showed negligible current in the absence of water, indicating that water was responsible for the observed reduction current (Fig. 2F). Control experiments also confirmed the critical role of water reduction in PVDF defluorination (fig. S17). No defluorination of PVDF was observed in the absence of water, underscoring its necessity for the reaction (fig. S17A). Similarly, when water was present, but its electrochemical reduction was prevented, no PVDF defluorination occurred, demonstrating that the reduction step is vital (fig. S17A). When the reaction was conducted in an H-type cell with water present, the cathode compartment turned black due to the formation of carbonaceous materials, and fluoride ions were detected in the catholyte, while no fluoride was found in the anode compartment (fig. S17B), further confirming that water acts as the essential electroactive species via $2H_2O + 2e^- \rightarrow H_2 + 2OH^-$ and ruling out the participation of anodic species in the defluorination reaction. On the basis of the abovementioned results, we hypothesized that the spatially confined, highly concentrated hydroxide ions near the electrode surface (Fig. 2A) act as the primary agent responsible for defluorination. To verify the presence of such concentrated hydroxide ions, phenolphthalein was introduced into the electrolyte. Upon application of potential, a distinct red coloration emerged near the cathode (movie S1), while the bulk solution remained colorless, visually confirming the spatial confinement of the hydroxide ion. The spatial distribution of OH^- was further investigated with scanning electrochemical microscopy (SECM), which showed that the OH^- was highly concentrated near the electrode (Fig. 2G). Transient voltage measurements (*35*) and in situ Raman spectroscopy quantified the surface concentration of OH^- to be approximately 0.13 M. Ab initio molecular dynamics (AIMD) simulations were used to determine the diffusion coefficient of OH^- in DMAc, after which the migration-diffusion equation was numerically solved (*36*). The resulting concentration profile showed good agreement with experimental data (Fig. 2H), further confirming the formation of a highly concentrated hydroxide ion layer at the electrode interface.

Defluorination mechanism analysis

The consistent performance across different electrodes confirmed a surface-insensitive mechanism (fig. S15). This was further supported by the fact that the defluorination of PVDF occurs in the absence of an applied potential when using TBAOH as the base (fig. S18). These results suggested that the defluorination reaction is occurring homogeneously in the electrolyte. On the basis of the above findings, we proposed that water served a dual function, acting as both a reactant and a catalyst in a unified water-mediated pathway that encompassed two distinct mechanisms: the water catalysis pathway and the water reaction pathway. Isotopic tracer experiments together with controlled experiments provided evidence validating this hypothesis.

Water catalysis pathway

Electrochemical reduction of water generated H_2 and hydroxide ions, while the latter reacted with PVDF and was regenerated as water. In this scenario, when D_2O was used in place of H_2O, D_2 would be generated initially. As the reaction proceeded, hydrogen in PVDF gradually exchanged with deuterium via reacting with OD^- species, leading to the formation of HDO and eventually H_2O, which resulted in the subsequent generation of HD and even H_2 (Fig. 3A). Isotopic experiments confirmed the water catalysis pathway as assumed. During electrolysis, D_2 was detected initially, followed by HD after 50 s and H_2 after 115 s (Fig. 3B). Furthermore, the water content remained essentially unchanged before and after the reaction, and the turnover number (TON) of water was calculated to be 6.2, confirming its catalytic role (fig. S19) (*37*).

Water reaction pathway

Alternatively, electrogenerated hydroxide ions participated in nucleophilic addition or substitution with PVDF and were incorporated into the products. In this scenario, when $H_2{}^{18}O$ is used in place of $H_2{}^{16}O$, signals of ^{18}O could be detected in the product (Fig. 3C). As assumed, when using $H_2{}^{18}O$ instead of $H_2{}^{16}O$, the ^{18}O signal in the solid products increased by four orders of magnitude (Fig. 3D), providing direct evidence of oxygen incorporation from water. Furthermore, the presence of oxygen-containing functional groups (C═O and C─OH) as confirmed by XPS (Fig. 2B) and elemental analysis showing an oxygen content of 12.5% also demonstrated the transfer of oxygen from water to the defluorinated polymer.

To elucidate the defluorination mechanism, we identified all possible reaction pathways and determined the corresponding activation free energies using density functional theory (DFT) (Fig. 4A). Same-type reactions involving reactants with different chemical formulae exhibited similar activation barriers, as reflected by minimal variance (less than 0.2 eV) across different reactant models. The activation energies for each reaction category were averaged to obtain a representative value. These pathways were classified into five major types, as summarized in Fig. 4A.

Given the higher complexity of polymer defluorination compared to small-molecule PFAS, we performed kinetic Monte Carlo simulations (*38*, *39*) using the rejection-free Bortz-Kalos-Lebowitz algorithm (*40*) to study the defluorination process. The overall simulation workflow is depicted in Fig. 4B (see fig. S20 and note S2 for full details). The simulated fluorine content decreased progressively over time. In the early stages, low-energy-barrier acid-base reactions dominated, wherein hydroxide ions extract protons from PVDF to form carbanion intermediates, subsequently triggering elimination reactions. At later stages, higher-energy pathways, specifically nucleophilic addition and substitution, became prevalent, leading to oxygen incorporation and the formation of C─OH and C═O bonds (Fig. 4C). The acid-base reactions align with the water catalysis pathway, while nucleophilic substitution and addition correspond to the water reaction pathway. The elemental composition of the simulated products agreed well with experimental values (Fig. 4D). The simulations indicated that the water catalysis pathway accounted for approximately 60% of the reactions, and the water reaction pathway contributed around 25% (Fig. 4E), demonstrating that both mechanisms participate at comparable levels in the defluorination process.

Scaled-up experiments for real battery PVDF defluorination

Considering that PVDF is the most commonly used binder in the electric vehicle battery, whose market size is projected to grow rapidly from 0.24 million metric tons in 2020 to approximately 3.5 million metric tons by 2030 in China, while its recycling technologies, however, remain underdeveloped, with only 20 to 30% undergoing appropriate recycling treatment (*2*), we performed validation experiments using real spent lithium-ion batteries to evaluate the practicability of the electrochemical defluorination strategy (Fig. 5A). The process started with mechanical disassembly of the battery and careful separation of the cathode material (NCM523) from the aluminum current collector. The harvested powder was thoroughly scraped off and dispersed in DMAc to achieve a PVDF concentration of approximately 0.1 M, as determined by ^{19}F–nuclear magnetic resonance (NMR)

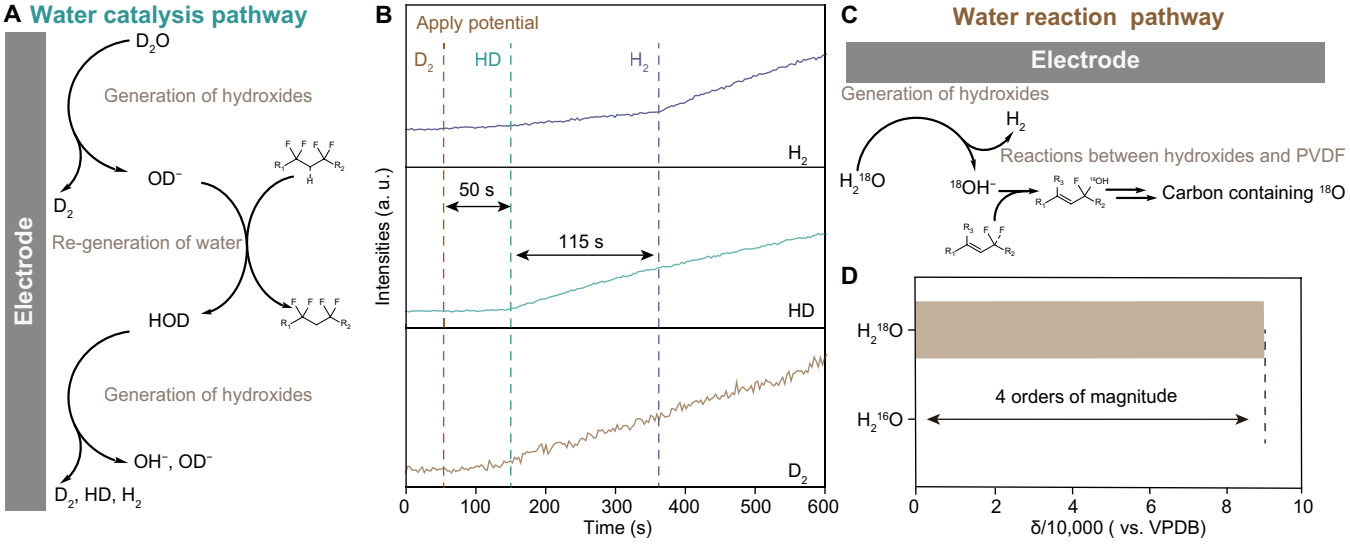

Fig. 3. Validation of the water-mediated pathway. (**A**) Illustration of the water catalysis pathway when using D_2O. (**B**) Isotopic experiments using D_2O. (**C**) Illustration of the water reaction pathway when using $H_2{}^{18}O$. (**D**) Comparison of using $H_2{}^{18}O$ and $H_2{}^{16}O$.

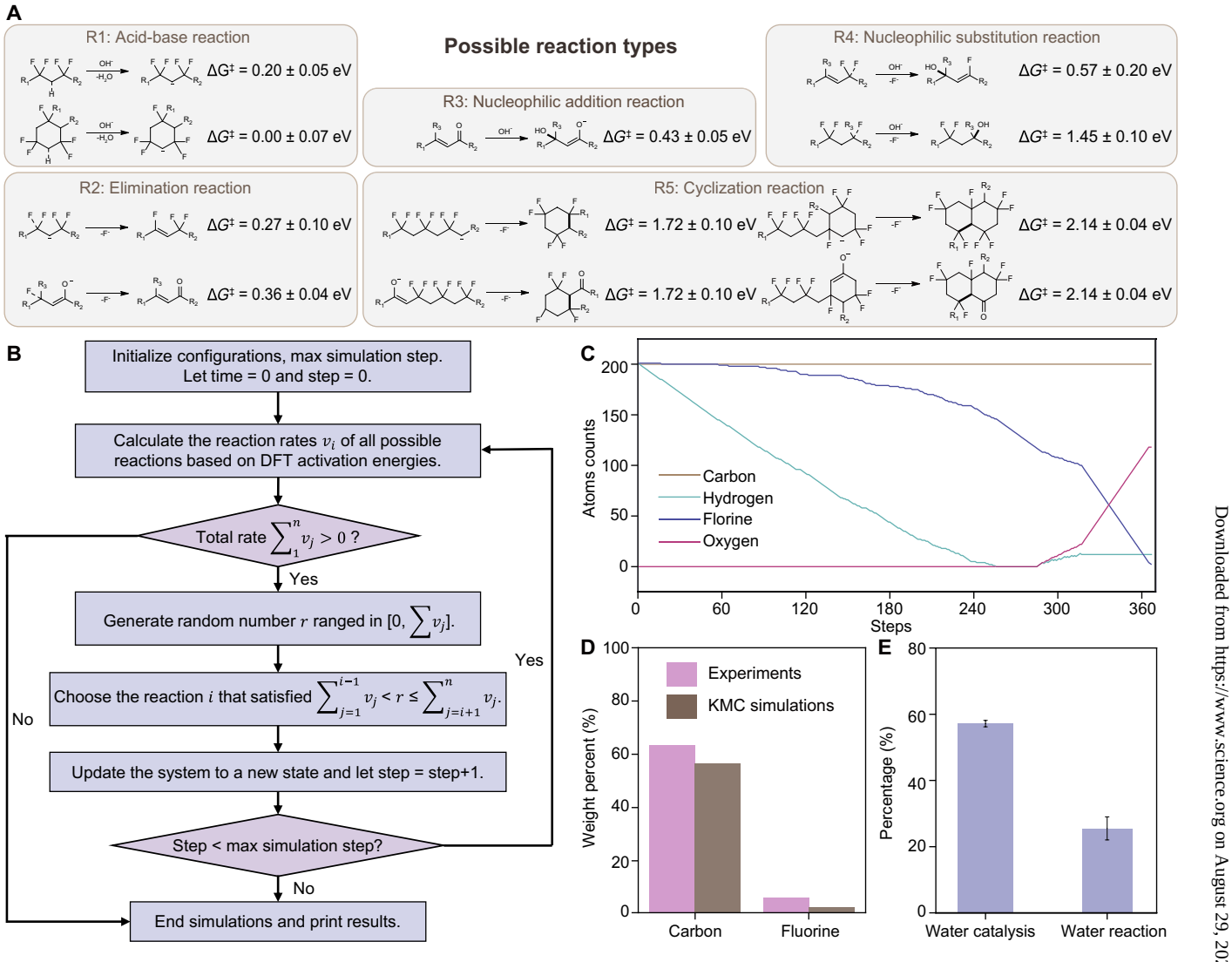

Fig. 4. Mechanism analysis. (**A**) Proposed possible reactions. (**B**) Scheme of rejection-free kinetic Monte Carlo simulations. (**C**) The evolution of different elements versus simulation steps during single simulations. (**D**) Element composition of the final simulated products and experimental results. (**E**) Proportions of the water catalysis pathway and water reaction pathway averaged over 48 simulations.

spectroscopy (fig. S21). Water was then introduced to a concentration of 0.5 M, along with tetrabutylammonium bromide (TBAB) as a supporting electrolyte at 0.2 M. Electrochemical defluorination was conducted under a constant current density of 20 mA cm^{-2} and a cell voltage of 3.8 V (Fig. 5A). After 11 hours of operation, 80% of the fluorine originally contained in the PVDF binder was converted to fluoride ions (Fig. 5B). The system exhibits impurity tolerance, delivering consistent performance under different simulated environmental impurities (fig. S22). In contrast, pyrolysis failed to effectively defluorinate PVDF into fluoride ions, achieving a defluorination efficiency of only 12% (Fig. 5B), substantially lower than that of the water-mediated process.

Notably, 98.1% (calculated on the basis of the mass, Fig. 5A) of the valuable cathode material was recovered, indicating minimal process loss and high compatibility with battery recycling. The structural and chemical integrity of the recovered electrode material was well preserved. XPS confirmed the unaltered valence states of key elements: lithium was primarily present in the 0 to +1 oxidation state, nickel exhibited a mixed valence of +2 and +3, cobalt remained in the +2 state, and manganese retained the +4 state, all consistent with the pristine cathode material (fig. S23) (*41*). Moreover, XRD analysis showed that the crystal structure of the electrode material following water-mediated defluorination retained the original framework without detectable phase degradation, whereas the structure collapsed after the conventional pyrolysis (fig. S24). Postreaction performance further validated the structural stability of the electrode materials, specifically, the capacity remained consistent, displaying a deviation of less than 2% before and after defluorination (fig. S25). The preservation of both chemical states and crystallinity underscored the mild yet highly effective nature of the electrochemical approach, which selectively degraded the PVDF binder without compromising the valuable cathode active material.

To further evaluate the scalability of the water-mediated defluorination strategy, we conducted scale-up experiments in a customized

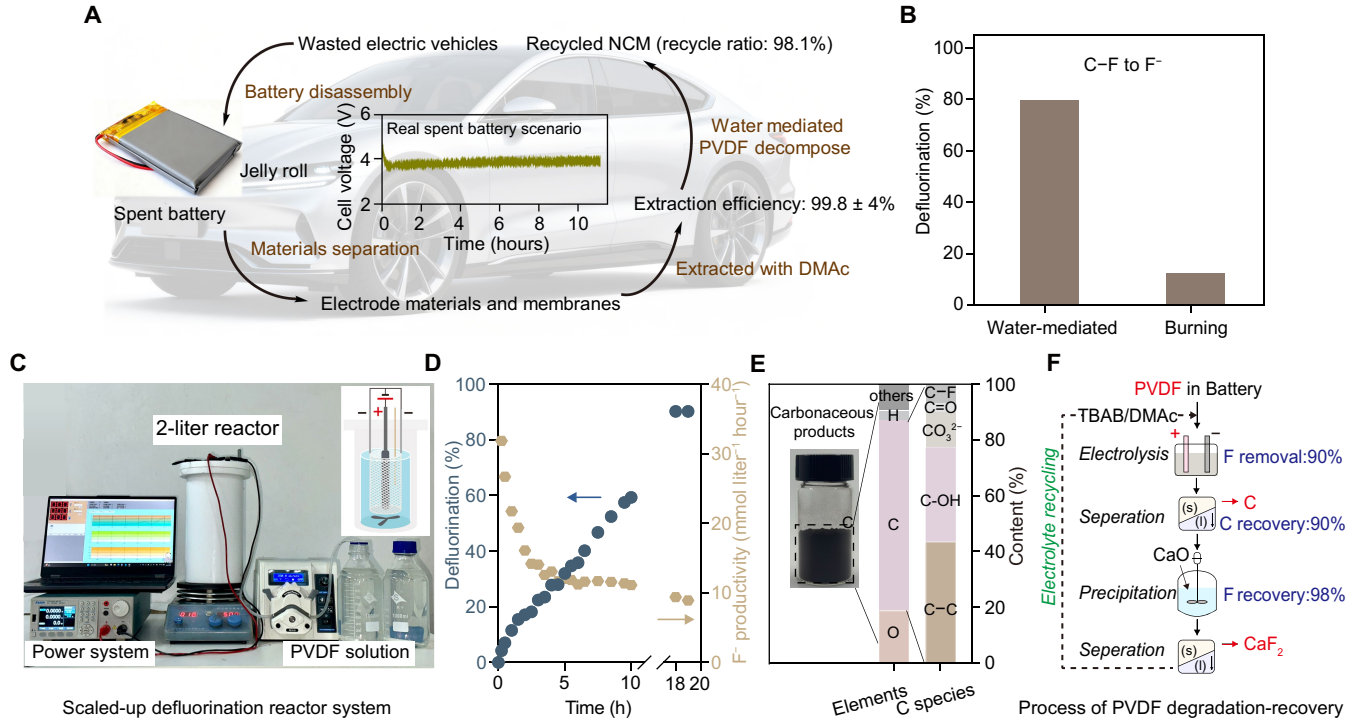

Fig. 5. Scaled-up PVDF defluorination for real lithium batteries. (**A**) Scheme of the defluorination process and the cell voltage. (**B**) Comparison of water-mediated PVDF defluorination and burning in terms of defluorination. (**C**) Digital photograph of the scaled-up defluorination reactor system (inset: detailed reactor configuration). (**D**) Defluorination and F^- productivity during reactor operation. (F^- productivity denotes the cumulative average from time zero to each data point). (**E**) Analysis of the carbonaceous products. (**F**) Scheme of the PVDF degradation and recovery process.

reactor with a working volume of 2 liters (Fig. 5C). The reaction was carried out at room temperature under a constant current of 2.5 A, with a corresponding cell voltage of approximately 8 V (fig. S26). As the reaction progressed, the color of the electrolyte transitioned from transparent to dark brown and finally to black, visually indicating the breakdown of PVDF and formation of carbonaceous products (fig. S27). After 18 hours of operation, a defluorination of 90% was achieved, corresponding to a final productivity of 8.9 mmol $liter^{-1}$ $hour^{-1}$ (Fig. 5D). Further performance enhancements may be realized through the implementation of H-type cells or the development of more chemically stable solvents (fig. S9 and table S1). Postreaction XPS analysis showed that the solid products exhibited a C/F atomic ratio of 336, while in pristine PVDF the ratio was approximately 1, confirming the efficient defluorination (fig. S28). Fluorine was predominantly converted to F^-, with minimal residual C—F bonds (less than 4%) present mainly as $[—CH=CF—]_n$ units (fig. S29). In addition, oxygen-containing functional groups such as hydroxyls and carbonyls were incorporated into the carbon matrix (Fig. 5F and fig. S30). From an initial input of 12.8 g of PVDF (4.8 g carbon), we obtained 6.3 g of oxygen-functionalized carbonaceous material (68.4 weight % carbon), achieving a carbon balance of 90% (Fig. 5E). The carbonaceous solid could further be used as the catalyst support for fuel cells due to the suppressed two-electron pathway (fig. S31). When normalized by the reactor volume and operation time, the PVDF treatment capacity reached 8.5 kg m^{-3} day^{-1}, equivalent to the PVDF in approximately 2 Tesla Model Y battery packs (see calculations in note S3). The electrode structures were characterized via scanning electron microscopy, XPS, and XRD before and after the reaction. No discernible structural changes were detected (figs. S32 to S34). These results highlight the excellent scalability of the water-mediated defluorination process under mild conditions.

The postreaction solution can be facilely regenerated through a precipitation/separation process (Fig. 5F). Oxygenated carbon was first removed via microfiltration, and fluoride ions were subsequently precipitated as CaF_2 by the addition of calcium oxide, achieving 98% fluoride recovery. After filtration, the solution was converted back to a reusable electrolyte. The inactive nature of the electrolyte, including DMAc and TBAB, was confirmed by ^{1}H-NMR, ^{13}C-NMR, and gas chromatography–mass spectrometry in figs. S35 to S37. This straightforward regeneration process further underscores the recyclability of the electrolyte, enabling sustainable operation of the water-mediated defluorination system towards scale-up implementations. The stability of the reactor was further confirmed through four consecutive reactions, all of which maintained a defluorination efficiency exceeding 90%. These results further demonstrate that the solvent remains highly effective for defluorination even after undergoing filtration and recycling (fig. S38). On the basis of the workflow proposed in Fig. 5F, our strategy demonstrates a processing cost of 166 USD per electric vehicle (fig. S39) and achieves a 70% reduction in global warming potential under the current energy mix, which is projected to decrease even further as the energy structure transitions toward renewable sources (fig. S40).

DISCUSSION

As PFASs, the environmental persistence of PVDF intensifies ecological and health concerns, highlighting an urgent need for safe and efficient defluorination techniques. Our electrochemical strategy

provides a unique and sustainable pathway for PVDF degradation under mild conditions through a synergistic combination of electrochemical and chemical processes, effectively bridging the gap between laboratory research and industrial application. In this system, water served a dual function as both reactant and catalyst, as confirmed through isotopic labeling and kinetic Monte Carlo simulations. We further demonstrated the industrial potential of our process by achieving a processing capacity of 8.5 kg m^{-3} day^{-1}. This rate, equivalent to two Tesla Model Y battery packs per m^3 of electrolyte per day, confirms the feasibility of large-scale recycling with real spent electrodes while ensuring the complete preservation of the material's integrity. This work efficiently defluorinated PVDF and achieved complete elimination of VFCs releases, demonstrating the potential in real wasted PVDF degradation scenarios without greenhouse gas emissions.

MATERIALS AND METHODS

Performance evaluation

The concentration of PVDF was calculated on the basis of the molecular weight of the monomer. PVDF (6.402 g) and TBAB (32.24 g) were dissolved in 1 liter of DMAc to reach the concentrations of 0.1 M. Platinum plates (area = 0.5 cm^2) were cleaned by successive washing in aqua regia, deionized water, ethanol, and acetone, followed by drying, before being used as both the anode and cathode. A 10-ml aliquot of electrolyte was used for each reaction, under a two-electrode configuration. Electrolysis was carried out in chronopotentiometry mode using a Princeton 2000 workstation. The reaction was carried out in a 15-ml PTFE electrolyzer under Ar protection. Before the chronopotentiometry tests, impedance spectra were recorded at open-circuit potential. For kinetic and mechanistic studies, reactions were restricted to the initial stage by limiting the passed charge to 5% of the total charge required for complete degradation. For full-conversion experiments, samples were collected periodically during the process to ensure that the fluoride ion concentration no longer changed over time.

After the reaction, the solution was diluted with water to reach a concentration of 1 to 50 parts per million depending on the estimation of the extent of defluorination in a plastic tube, and quantitatively analyzed for fluoride ions using ion chromatography (DIONEX ICS-1100) with the external standard method. The solution shall avoid contacting any glass materials. The standard curve is shown in fig. S41. The column (DIONEX IONPAC AS23) was maintained at 30°C, and the eluent flow consisted of a Na_2CO_3/$NaHCO_3$ buffer solution with concentrations of 4.5 mM sodium carbonate and 0.8 mM sodium bicarbonate. The eluent flow rate was 1 ml min^{-1}, and the column pressure was approximately 2000 psi.

In addition, ^{19}F-NMR was used as a complementary method to validate the concentrations determined by ion chromatography (fig. S42). It is important to note that a relaxation delay of more than 20 s was required to achieve quantitative equilibrium (fig. S43). Furthermore, the etching of the NMR tubes by fluoride ions proved unavoidable during the measurement process.

The FE was calculated by

$$\text{FE}\,(\%) = \frac{n_{F^-}F}{Q} \times 100\,\%$$

where n_{F^-} is the amount of F^- (mol), F is the Faraday constant (96,485 C mol^{-1}), and Q is the quantity of electric charge (C).

The conversion of fluorine to F^- was calculated by

$$\text{Conversion} = \frac{n_{F^-}}{2n_{\text{PVDF}}}$$

where n_{F^-} is the amount of F^- (mol) and n_{PVDF} is the amount of PVDF (mol) calculated by the repeat unit.

To obtain accurate carbon and fluorine balances, we scaled up the reaction preliminarily and modified the composition of the electrolyte. In this process, 640 mg of PVDF was dissolved in 100 ml of DMAc, with a TBAB concentration of 0.2 M. The calculation formula for the fluorine balance in this process is

$$\text{Fluorine balance} = \frac{n_{F^-}}{2n_{\text{PVDF}}}$$

where n_{F^-} is the amount of F^- (mol) and n_{PVDF} is the amount of PVDF (mol) calculated by the repeat unit.

The raw product was dispersed in a sevenfold volume excess of water and subjected to centrifugation at 12,000 rpm, followed by five consecutive washing cycles with pure water. The calculation formula for the carbon balance in this process is

$$\text{Carbon balance} = \frac{wm}{24n_{\text{PVDF}}}$$

where m is the mass (g) of the final solid product, w is the weight percentage of carbon in the final solid product, and n_{PVDF} is the amount of PVDF (mol) calculated by the repeat unit. The carbon content in the solid products was determined using a CHN analyzer (Vario EL cube).

The TON was calculated by

$$\text{TON} = \frac{n_{F^-}}{n_{H_2O}^{\text{initial}} - n_{H_2O}^{\text{final}}}$$

where n_{F^-} is the amount of F^- (mol), $n_{H_2O}^{\text{initial}}$ is the initial amount of H_2O (mol) and $n_{H_2O}^{\text{final}}$ is the final amount of H_2O (mol).

The solvent used for linear sweep voltammetry was dehydrated using 3-Å molecular sieves. Platinum rotating disk electrode was used as the working electrode, graphite rod as the counter electrode, and Ag/AgCl electrode as the reference electrode. The potential was calibrated with ferrocene (Fc) and calculated versus Fc/Fc^+. The scan rate was 10 mV s^{-1}. All data presented in the manuscript were corrected for IR drop by electrochemical impedance spectroscopy.

Characterization

XRD patterns were collected with PANalytical X-Pert3 Powder X-ray diffractometer, using Cu Kα (λ = 0.15418 nm) as the radiation source. XPS were recorded from AXIS Supra X-ray Photoelectron Spectrometer with Al/Mg Kα X-rays as the excitation source. Infrared spectroscopy was collected with Bruker Tensor 27. ^{18}O was tested with an isotope ratio mass spectrometer (Thermo Delta V Advantage).

Measurement and simulations of the local pOH

Measuring the value of local pOH near the electrode experimentally relied on transient voltage measurements and in situ Raman spectroscopy. The transient voltage measurements were conducted in Faraday cages with a time resolution of 0.1 ms. The basic principles of which have been described elsewhere in detail (*35*). In our system, the bulk pH was measured using a pH meter. When the circuit was abruptly disconnected, both the discharging of the electric double layer and potential changes due to localized diffusion occurred, with these

two processes differing substantially in their timescales. Immediately after cutting off the applied voltage, the hydroxide ions enriched at the electrode surface caused a voltage shift that varied with the diffusion time of the hydroxide ions. When diffusion reached equilibrium, the hydroxide ion concentration at the electrode surface became consistent with that in the bulk solution, and the open circuit potential remained stable. On the basis of the Nernst equation, the difference in OH^- concentration between the electrode surface and the bulk solution at the moment of cutting off the applied voltage could be calculated. We shall note here that the ion concentration is assumed to approximate its activity.

Specific molecules could serve as pH probes, as their Raman peak positions and intensities shift in response to hydroxide concentration (*42*). Accounting for the interference of solvent and TBAB peaks, we selected 4-ethynylpyridine (fig. S44A) as the probe molecule (*43*). In its Raman spectra, the ratio of the peak intensities at 2080 cm^{-1} to the total intensities of the 2080 and 2010 cm^{-1} peaks [$I_{2080}/(I_{2080} + I_{2010})$] correlates with hydroxide concentration (fig. S44B). Accordingly, we established a calibration curve by measuring the intensity ratio across a range of known hydroxide concentrations under nonelectrochemical conditions (fig. S44C). Upon adding 4-ethynylpyridine to our experimental system, we recorded a ratio of 0.4363 at 10 mA cm^{-2}, corresponding to a calculated OH^- concentration of 0.138 M based on the calibration curve (Fig. 2H).

To obtain the diffusion coefficient of OH^- in DMAc, 10 ps AIMD simulations were conducted at 298.15 K using canonical NVT ensembles with Nosé-Hoover thermostat. The convergence was confirmed by the energy (fig. S45A). The model was constructed on the basis of the density and concentration of the electrolyte, comprising 16 DMAc molecules, 1 OH^-, and 1 H_2O molecule. A TBA^+ ion was introduced to balance the charge of OH^-. Structural snapshots at 10 ps are shown in fig. S45B. After the 10 ps simulation, the geometric structure remained intact, indicating its thermal stability. The diffusion coefficient of OH^- was calculated by

$$D = \frac{1}{6}\mathrm{MSD}t$$

where t is simulation time (s), MSD is the mean square displacement of OH^- (m^2).

The distribution of hydroxide ions at the electrode surface was numerically simulated by solving the migration-diffusion equation

$$J_i = -D_i\frac{\mathrm{d}c_i}{\mathrm{d}x} - \frac{z_i F D_i}{RT}c_i\frac{\mathrm{d}\phi}{\mathrm{d}x}$$

where J is the molar flux (mol m^{-2} s^{-1}), c is the concentration of the diffusing substance (mol m^{-3}), x is the position coordinate (m), and D is the diffusion coefficient (m^2 s^{-1}), which was obtained by AIMD, z is the number of the charge that the species carries, F is the Faraday constant (96485 C mol^{-1}), R is the gas constant (8.314 J mol^{-1} K^{-1}), and ϕ is the electrostatic potential (V).

The electroneutrality principle

$$c_{TBA^+} = c_{Br^-} + c_{OH^-}$$

Thus, there exist four functions to solve four parameters c_{OH^-}, c_{TBA^+}, c_{Br^-}, and ϕ.

The assumptions and the boundary conditions to solve the migration-diffusion equation are summarized here and the entire procedure is programmed in Python:

1) The system reaches the steady state. The characteristic time is estimated to be 30 s to 1 min. Thus, the system reaches the steady state within our experiment time (~15 min to ~20 hours).

2) The problem is a one-dimensional problem. Near the electrode x equals 0, and at the diffusion layer boundary x equals δ (*35*).

3) Inside the diffusion layer, there is no convection.

4) $J_{OH^-} = j/F$ at $x = 0$. $J_{Br^-} = 0$ and $J_{TBA^+} = 0$ at $x = 0$ because Br^- and TBA^+ does not involved in the electrochemical reaction.

5) At $x = \delta$, $c_{TBA^+} = c_{Br^-} = 0.1$ M, $c_{OH^-} = 0$, and $\phi = 0$.

6) The diffusion layer boundary is measured with SECM.

The spatial distribution of OH^- is measured with SECM. Specifically, a Pt/IrO_2 (*44*) microelectrode (25 μm) was used in a four-electrode configuration to map the concentration gradient. The underlying principle relies on the potential shift between the probe and the reference electrode in response to varying hydroxide concentrations. By using a stepper motor to precisely control the distance between the probe and the working electrode, we can resolve the local OH^- concentration at different positions. The probe was positioned at the working electrode surface using feedback mode to detect the potential surge, after which its displacement was controlled while recording the potential.

DFT calculations

Geometry optimizations, frequency analyses, and single-point energies were performed at the M06-2X/6-311+G(2d,p)-SMD-(DMAc) level using the Gaussian 16 package, using the convergence criteria of maximum force <0.00045 a.u., root mean square (RMS) force <0.00030 a.u., maximum displacement <0.00180 a.u., and RMS displacement <0.00120 a.u (*45*, *46*). No imaginary frequency was found for the reactants, products, and intermediates, while only one imaginary frequency toward the product from the reactant was found for the transition state. The unit of energy is eV unless otherwise noted.

Kinetic Monte Carlo simulations

We got the rate constants with the Eyring equation

$$k = \frac{k_B T}{h}\exp\left(-\frac{\Delta G^{\ddagger}}{RT}\right)$$

where k_B is the Boltzmann constant (1.38×10^{-23} J K^{-1}), T is the temperature (K), h is Planck's constant (6.626×10^{-34} J s), $\Delta G^{\ddagger}$ is the Gibbs energy of activation (J mol^{-1}), and R is the gas constant (8.314 J mol^{-1} K^{-1}). The rate of the element reaction was derived from the mass action law

$$v = k\prod C_i^{n_i}$$

where C_i is the concentration of reactant i and n_i is the stoichiometric coefficient of reactant i.

Kinetic Monte Carlo used the rejection-free Bortz-Kalos-Lebowitz algorithm. The program was implemented with Python. All the data shown were repeated 48 times, and we used the average of the results unless otherwise noted. More detailed analysis was shown in note S2.

In situ isotopic experiment

In situ isotopic experiments were carried out using argon as the carrier at 80°C. Platinum plates (area = 0.5 cm^2) were used as both the anode and cathode. Before the reaction, the electrochemical cell was purged continuously with pure Ar gas to remove the residual gas. We analyzed the outlet gas using the SRS RGA 200 mass spectrometer

online MS, and focused on the component using the following mass spectrum signals: H_2 ($m/z = 2$), D_2 ($m/z = 4$), and HD ($m/z = 3$). We applied the online measured inert gas signal, Ar ($m/z = 40$), as the benchmark to normalize the flow rate for calculating the relative concentration of each component.

Large-scale PVDF defluorination

The large-scale PVDF defluorination reactor had a total capacity of 3 liters (an internal diameter of 120 mm and a height of 270 mm) and an effective solution volume of 2 liters. The electrolyte consisted of 0.2 M TBAB, 0.5 M water, and 0.1 M PVDF with DMAc as the solvent. The electrodes were configured in a coaxial geometry. The anode was a Ru-Ir/Ti dimensionally stable anode (a diameter of 30 mm and a height of 160 mm), placed at the center of the reactor. The cathode was a Pt/Ti mesh electrode (a diameter of 100 mm and a height of 160 mm, with a mesh size of 1 × 3 mm), positioned concentrically around the anode. To ensure uniform current distribution, two conductive rods were connected to the cathode. The reaction was performed at room temperature with a constant current of 2.5 A supplied by a DC power source (DP305C, Mestek, China). The corresponding cell voltage was recorded during operation. The electrolyte was stirred magnetically at 500 rpm to maintain homogeneous mixing and efficient mass transfer. At predetermined intervals, 1-ml aliquots of the electrolyte were withdrawn for fluoride ion concentration analysis. Upon completion of electrolysis, the mixture was subjected to vacuum filtration to separate the solid products from the liquid phase. The solid fraction was thoroughly washed several times with DMAc and deionized water to remove residual electrolyte, and subsequently analyzed by XPS and elemental analysis. Fluoride ions in the filtrate were recovered by the addition of excess calcium oxide, which precipitated fluoride as CaF_2. The solution was subsequently filtered to remove the precipitate, yielding a regenerated TBAB/DMAc electrolyte suitable for reuse.

Real battery PVDF defluorination

The cathode material was disassembled physically from the spent battery in a glove box. Then, the entire electrode material was scratched from the aluminum foil and immersed in DMAc, stirring with ultrasonication for 24 hours. Subsequently, we quantitatively determined the PVDF content using ^{19}F-NMR (fig. S21). The mixture was diluted to reach the PVDF concentration of 0.1 M, and TBAB was added to reach a concentration of 0.1 M as the supporting electrolyte, along with water to reach the concentration of 0.5 M. Platinum plates were used as both the cathode and anode. Electrolysis was performed under chronoamperometry mode at a current density of 20 mA cm^{-2} for 11 hours. After the reaction, the concentration of F^- in the solution was quantified using ion chromatography. The recycle ratio of the electrode material was calculated as the ratio of the mass of the washed product after the reaction to the initial value, which is obtained by multiplying the mass of the waste battery material before the reaction by its content.

Supplementary Materials

The PDF file includes:
Supplementary Text
Figs. S1 to S45
Table S1
Legend for movie S1
References

Other Supplementary Material for this manuscript includes the following:
Movie S1

REFERENCES

1. D. Castelvecchi, Electric cars and batteries: How will the world produce enough? *Nature* **596**, 336–339 (2021).
2. A. Sinha, J. Wu, China needs to deal with discarded electric-vehicle batteries. *Nature* **641**, 594 (2025).
3. X. Yang, H. Zhang, Q. Liu, G. Jiang, The Li-ion battery industry and its challenges. *Nat. Rev. Chem.* **9**, 497–498 (2025).
4. X. Ma, Z. Meng, M. V. Bellonia, J. Spangenberger, G. Harper, E. Gratz, E. Olivetti, R. Arsenault, Y. Wang, The evolution of lithium-ion battery recycling. *Nat. Rev. Clean Technol.* **1**, 75–94 (2025).
5. J. Lopez, D. G. Mackanic, Y. Cui, Z. Bao, Designing polymers for advanced battery chemistries. *Nat. Rev. Mater.* **4**, 312–330 (2019).
6. R. Dallaev, T. Pisarenko, D. Sobola, F. Orudzhev, S. Ramazanov, T. Trcka, Brief review of PVDF properties and applications potential. *Polymers* **14**, 4793 (2022).
7. P. Lott, F. Maurer, A. Beck, Roadmap to catalytic abatement of gas phase per- and polyfluoroalkyl substances (PFAS). *Angew. Chem. Int. Ed. Engl.* **64**, e202424718 (2025).
8. S. C. E. Leung, D. Wanninayake, D. Chen, N.-T. Nguyen, Q. Li, Physicochemical properties and interactions of perfluoroalkyl substances (PFAS) - Challenges and opportunities in sensing and remediation. *Sci. Total Environ.* **905**, 166764 (2023).
9. R. E. Ciez, J. F. Whitacre, Examining different recycling processes for lithium-ion batteries. *Nat. Sustain.* **2**, 148–156 (2019).
10. H. Ji, J. Wang, X. Qiu, H. Ren, H. Xue, H. Zhang, G. Ji, H.-M. Cheng, G. Zhou, A universal protocol for ultrafast direct regeneration and upcycling of spent lithium-ion battery cathode materials. *Nat. Protoc.* **21**, 2413–2447 (2025).
11. A. Sarkar, R. May, S. Ramesh, W. Chang, L. E. Marbella, Recovery and reuse of composite cathode binder in lithium ion batteries. *ChemistryOpen* **10**, 545–552 (2021).
12. J. L. Guelfo, P. L. Ferguson, J. Beck, M. Chernick, A. Doria-Manzur, P. W. Faught, T. Flug, E. P. Gray, N. Jayasundara, D. R. U. Knappe, A. S. Joyce, P. Meng, M. Shojaei, Lithium-ion battery components are at the nexus of sustainable energy and environmental release of per- and polyfluoroalkyl substances. *Nat. Commun.* **15**, 5548 (2024).
13. H. Wang, M. Rehwoldt, D. J. Kline, T. Wu, P. Wang, M. R. Zachariah, Comparison study of the ignition and combustion characteristics of directly-written Al/PVDF, Al/Viton and Al/THV composites. *Combust. Flame* **201**, 181–186 (2019).
14. Y. Ji, C. T. Jafvert, N. N. Zyaykina, F. Zhao, Decomposition of PVDF to delaminate cathode materials from end-of-life lithium-ion battery cathodes. *J. Clean. Prod.* **367**, 133112 (2022).
15. C. Austin, A. L. Purohit, C. Thomsen, B. R. Pinkard, T. J. Strathmann, I. V. Novosselov, Hydrothermal destruction and defluorination of trifluoroacetic acid (TFA). *Environ. Sci. Technol.* **58**, 8076–8085 (2024).
16. B. Trang, Y. Li, X.-S. Xue, M. Ateia, K. N. Houk, W. R. Dichtel, Low-temperature mineralization of perfluorocarboxylic acids. *Science* **377**, 839–845 (2022).
17. C. Patel, E. André-Joyaux, J. A. Leitch, X. M. D. Irujo-Labalde, F. Ibba, J. Struijs, M. A. Ellwanger, R. Paton, D. L. Browne, G. Pupo, S. Aldridge, M. A. Hayward, V. Gouverneur, Fluorochemicals from fluorspar via a phosphate-enabled mechanochemical process that bypasses HF. *Science* **381**, 302–306 (2023).
18. T. Araki, H. Ota, Y. Murata, Y. Sumii, J. Hamaura, H. Adachi, T. Kagawa, H. Hori, J. Escorihuela, N. Shibata, Room-temperature defluorination of PTFE and PFAS via sodium dispersion. *Nat. Commun.* **16**, 6526 (2025).
19. L. Yang, Z. Chen, C. A. Goult, T. Schlatzer, R. S. Paton, V. Gouverneur, Phosphate-enabled mechanochemical PFAS destruction for fluoride reuse. *Nature* **640**, 100–106 (2025).
20. M. Hattori, D. Saha, M. Z. Bacho, N. Shibata, Mechanochemical pathway for converting fluoropolymers to fluorochemicals. *Nat. Chem.* **17**, 1480–1487 (2025).
21. H. Zhang, J.-X. Chen, J.-P. Qu, Y.-B. Kang, Photocatalytic low-temperature defluorination of PFASs. *Nature* **635**, 610–617 (2024).
22. X. Liu, A. Sau, A. R. Green, M. V. Popescu, N. F. Pompetti, Y. Li, Y. Zhao, R. S. Paton, N. H. Damrauer, G. M. Miyake, Photocatalytic C–F bond activation in small molecules and polyfluoroalkyl substances. *Nature* **637**, 601–607 (2024).
23. S. Yin, J. J. Calvillo Solis, C. Sandoval-Pauker, D. Puerto-Diaz, D. Villagran, Advances in PFAS electrochemical reduction: Mechanisms, materials, and future perspectives. *J. Hazard. Mater.* **491**, 137943 (2025).
24. B. Sarkar, R. L. Kumawat, P. Ma, K. H. Wang, M. Mohebi, G. C. Schatz, C. V. Amanchukwu, Lithium metal-mediated electrochemical reduction of per- and poly-fluoroalkyl substances. *Nat. Chem.* **18**, 509–518 (2026).
25. J. J. Calvillo Solis, C. Sandoval-Pauker, D. Bai, S. Yin, T. P. Senftle, D. Villagran, Electrochemical reduction of perfluorooctanoic acid (PFOA): An experimental and theoretical approach. *J. Am. Chem. Soc.* **146**, 10687–10698 (2024).

26. J. Wu, L. Xu, Z. Kong, K. Gu, Y. Lu, X. Wu, Y. Zou, S. Wang, Integrated tandem electrochemical-chemical-electrochemical coupling of biomass and nitrate to sustainable alanine. *Angew. Chem. Int. Ed. Engl.* **62**, e202311196 (2023).
27. C. Liu, F. Chen, B.-H. Zhao, Y. Wu, B. Zhang, Electrochemical hydrogenation and oxidation of organic species involving water. *Nat. Rev. Chem.* **8**, 277–293 (2024).
28. J. Ke, J. Zhao, M. Chi, M. Wang, X. Kong, Q. Chang, W. Zhou, C. Long, J. Zeng, Z. Geng, Facet-dependent electrooxidation of propylene into propylene oxide over Ag_3PO_4 crystals. *Nat. Commun.* **13**, 932 (2022).
29. M. A. Hoque, J. B. Gerken, S. S. Stahl, Synthetic dioxygenase reactivity by pairing electrochemical oxygen reduction and water oxidation. *Science* **384**, 173–178 (2024).
30. M. Chung, J. H. Maalouf, J. S. Adams, C. Jiang, Y. Román-Leshkov, K. Manthiram, Direct propylene epoxidation via water activation over Pd-Pt electrocatalysts. *Science* **383**, 49–55 (2024).
31. X. Xu, Y. Li, P. H. N. Vo, P. Shukla, L. Ge, C.-X. Zhao, Electrochemical advanced oxidation of per- and polyfluoroalkyl substances (PFASs): Development, challenges and perspectives. *Chem. Eng. J.* **500**, 157222 (2024).
32. B. T.-W. Tan, N. H. H. A. Bakar, H. L. Lee, Electrochemical methods for treatment of per- and polyfluoroalkyl substances (PFAS): A review. *J. Environ. Chem. Eng.* **13**, 114990 (2025).
33. Y. Wang, M. Wen, J. Han, Q. Chu, D. Chen, Pyrolysis kinetics of gas-phase polyvinylidene fluoride (PVDF): A DFT study. *Fuel* **405**, 136459 (2026).
34. T. Boccaccio, A. Bottino, G. Capannelli, P. Piaggio, Characterization of PVDF membranes by vibrational spectroscopy. *J. Membr. Sci.* **210**, 315–329 (2002).
35. E. R. Sauvé, B. Y. Tang, N. K. Razdan, W. L. Toh, S. Weng, Y. Surendranath, Open circuit potential decay transients quantify interfacial pH swings during high current density hydrogen electrocatalysis. *Joule* **8**, 728–745 (2024).
36. J. E. Huang, F. Li, A. Ozden, A. S. Rasouli, F. P. G. De Arquer, S. Liu, S. Zhang, M. Luo, X. Wang, Y. Lum, Y. Xu, K. Bertens, R. K. Miao, C.-T. Dinh, D. Sinton, E. H. Sargent, CO_2 electrolysis to multicarbon products in strong acid. *Science* **372**, 1074–1078 (2021).
37. K. J. Laidler, A glossary of terms used in chemical kinetics, including reaction dynamics. *Pure Appl. Chem.* **68**, 149–192 (1996).
38. D. T. Gillespie, Approximate accelerated stochastic simulation of chemically reacting systems. *J. Chem. Phys.* **115**, 1716–1733 (2001).
39. A. F. Voter, Hyperdynamics: Accelerated molecular dynamics of infrequent events. *Phys. Rev. Lett.* **78**, 3908–3911 (1997).
40. A. B. Bortz, M. H. Kalos, J. L. Lebowitz, A new algorithm for Monte Carlo simulation of Ising spin systems. *J. Comput. Phys.* **17**, 10–18 (1975).
41. H.-J. Guo, H.-X. Wang, Y.-J. Guo, G.-X. Liu, J. Wan, Y.-X. Song, X.-A. Yang, F.-F. Jia, F.-Y. Wang, Y.-G. Guo, R. Wen, L.-J. Wan, Dynamic evolution of a cathode interphase layer at the surface of $LiNi_{0.5}Co_{0.2}Mn_{0.3}O_2$ in quasi-solid-state lithium batteries. *J. Am. Chem. Soc.* **142**, 20752–20762 (2020).
42. A. Steinegger, O. S. Wolfbeis, S. M. Borisov, Optical sensing and imaging of pH values: Spectroscopies, materials, and applications. *Chem. Rev.* **120**, 12357–12489 (2020).
43. J. K. Lim, S.-W. Joo, Gold nanoparticle-based pH sensor in highly alkaline region at pH > 11: Surface-enhanced Raman scattering study. *Appl. Spectrosc.* **60**, 847–852 (2006).
44. J. Guo, R. Wang, Y. Yang, Q. Zhang, F. Cao, J. Zhao, C. Pan, T. Ling, Local alkalinity enables high-performance pure water anion exchange membrane electrolysis. *Nat. Commun.* **17**, 2335 (2026).
45. N. Mardirossian, M. Head-Gordon, How accurate are the Minnesota density functionals for noncovalent interactions, isomerization energies, thermochemistry, and barrier heights involving molecules composed of main-group elements? *J. Chem. Theory Comput.* **12**, 4303–4325 (2016).
46. M. J. Frisch, G. W. Trucks, H. B. Schlegel, G. E. Scuseria, M. A. Robb, J. R. Cheeseman, G. Scalmani, V. Barone, G. A. Petersson, H. Nakatsuji, X. Li, M. Caricato, A. V. Marenich, J. Bloino, B. G. Janesko, R. Gomperts, B. Mennucci, H. P. Hratchian, J. V. Ortiz, A. F. Izmaylov, J. L. Sonnenberg, D. Williams-Young, F. L. F. Ding, F. Egidi, J. Going, B. Peng, A. Petrone, T. Henderson, D. Ranasinghe, V. G. Zakrzewski, J. Gao, N. Rega, G. Zheng, W. Liang, M. Hada, M. Ehara, K. Toyota, R. Fukuda, J. Hasegawa, M. Ishida, T. Nakajima, Y. Honda, O. Kitao, H. Nakai, T. Vreven, K. Throssell, J. A. Montgomery, J. E. P. Jr., F. Ogliaro, M. J. Bearpark, J. J. Heyd, E. N. Brothers, K. N. Kudin, V. N. Staroverov, R. K. T. A. Keith, J. Normand, K. Raghavachari, A. P. Rendell, J. C. Burant, S. S. Iyengar, J. Tomasi, M. Cossi, J. M. Millam, M. Klene, C. Adamo, R. Cammi, J. W. Ochterski, R. L. Martin, K. Morokuma, O. Farkas, J. B. Foresman, D. J. Fox, I. Gaussian, Ed. (Wallingford CT, 2016).
47. J. Gorsch, J. Schneiders, M. Frieges, N. Kisseler, D. Klohs, H. Heimes, A. Kampker, M. Muñoz Castro, E. Siebecke, Contrasting a BYD blade prismatic cell and Tesla 4680 cylindrical cell with a teardown analysis of design and performance. *Cell Rep. Phys. Sci.* **6**, 102453 (2025).
48. Y. Zhao, Y. Kang, J. Wozny, J. Lu, H. Du, C. Li, T. Li, F. Kang, N. Tavajohi, B. Li, Recycling of sodium-ion batteries. *Nat. Rev. Mater.* **8**, 623–634 (2023).
49. B.-H. Lee, H. Shin, A. S. Rasouli, H. Choubisa, P. Ou, R. Dorakhan, I. Grigioni, G. Lee, E. Shirzadi, R. K. Miao, J. Wicks, S. Park, H. S. Lee, J. Zhang, Y. Chen, Z. Chen, D. Sinton, T. Hyeon, Y.-E. Sung, E. H. Sargent, Supramolecular tuning of supported metal phthalocyanine catalysts for hydrogen peroxide electrosynthesis. *Nat. Catal.* **6**, 234–243 (2023).
50. H. Liu, J. Han, Y. Feng, C. Nong, Y. Liu, L. Cheng, J. Gu, H. Yuan, Thermal decomposition characteristics, products, and thermal transformation mechanisms of fluorine-containing organic components in lithium-ion batteries. *J. Environ. Chem. Eng.* **13**, 120248 (2025).
51. K. Momma, F. Izumi, VESTA 3 for three-dimensional visualization of crystal, volumetric and morphology data. *J. Appl. Cryst.* **44**, 1272–1276 (2011).

Acknowledgments: We thank the High-Performance Computing Platform of Peking University for their support in the simulations. **Funding:** This work was supported by. National Key R&D Program of China 2024YFC3714900 (W.Y. and M.L.); National Natural Science Foundation of China grants 22372004 (M.L.), 52100021 (W.Y.), 22576002 (W.Y.), and 62488201 (S.D.); and Beijing Natural Science Foundation Z240027 (M.L.) **Author contributions:** Conceptualization: M.L., W.Y., and S.D. Methodology: Y.B., P.L., X.Y., and Y.X. Investigation: Y.B., P.L., X.Y., C.J., and J.X. Resources: Y.X. Validation: C.J.. Formal analysis: C.J. and L.T. Software: L.T. Visualization: Y.B., P.L., X.Y., and C.J. Supervision: M.L., W.Y., S.D., and Y.X. Writing–original draft: Y.B. and X.Y. Funding acquisition: W.Y. Project administration: W.Y. Writing–review and editing: M.L., W.Y., S.D., J.X., and L.T. **Competing interests:** The authors declare that they have no competing interest. **Data, code, and materials availability:** All data and code needed to evaluate and reproduce the results in the paper are present in the paper and/or the Supplementary Materials. This study did not generate new materials.

Submitted 5 March 2026
Accepted 17 July 2026
Published 28 August 2026
10.1126/sciadv.aeg8495

ScienceAdvances

Electrocatalytic polyvinylidene fluoride defluorination with water mediation at room temperature

Yifan Bu, Peixuan Li, Xiayu Yuan, Lei Tao, Chengcheng Ji, Junzhong Xie, Yao Xu, Shixuan Du, Wulin Yang, and Mufan Li

Sci. Adv. **12** (35), eaeg8495. DOI: 10.1126/sciadv.aeg8495

Science Advances (ISSN 2375-2548) is published by the American Association for the Advancement of Science. 1200 New York Avenue NW, Washington, DC 20005. The title *Science Advances* is a registered trademark of AAAS.